Study of ionic and electronic transport properties influencing the performance of Lithium-ion batteries

Internship Report/Master Thesis

by

Julius Akinribido

Surface, Electro-, Radiation, and Photo-Chemistry (SERP+)

January – July 2022.

Supervised by: **Olivier Dubrunfaut**
Loïc Assaud
Jean-Claude Badot

Table of Contents

Acknowledgments

I am grateful for the opportunity to join the Erasmus Mundus SERP+ Program. The experiences of the two-year master have set a landmark for my academic and professional careers.

My heartfelt thanks go to my thesis supervisor and co-supervisors, Dr. Olivier Dubrunfaut, Dr. Loïc Assaud, and Dr. Jean-Claude Badot, for their continuous guidance and support during the internship, and Prof. Sylvain Franger for his insightful comments.

I thank the Institut de l'Énergie Soutenable (IES Paris-Saclay) for the financial support of my project, as well as collaborating institutes, Institut de Chimie Moléculaire et des Matériaux d'Orsay (ICMMO) and Laboratoire de Génie électrique et électronique de Paris (GeePs), for the wonderful environment created to attempt high-quality research. Also, thanks to Serge Albacha, Anshuman Agrawal, Benjamin Rondeau, Yutzil Segura, Florian Guenard, Hadeer Khalifa, and other ERIEE team members, for their company and scientific discussions.

Special thanks to the director of the SERP+ program, Prof. Sandrine Lacombe, and the local coordinator from the University of Porto, Prof. Eduardo Marques, and also to the excellent staff team that efficiently delivered the master's program. I also appreciate the program manager, Eva Renouf, and secretary, Kali Sidibé, for providing prompt information and guidance throughout the master's program.

My appreciation goes to my home country professors, Prof. Folahan Adekola and Prof. Alafara Baba, for their incredible support and for providing the necessary foundation and inspiration to help their students achieve academic and research excellence.

Many thanks to my SERP+ colleagues for their encouragement and support, and to my friends, Ademola Adeniji, Raj Shekhar, Nitik Bhatia, Merin Kennedy, and Kiran Hidayat, for the great moments we shared. To my mother, Feyisayo, and siblings – Ademola, Victoria, and Itunu, for always supporting me.

Abstract

A major factor in optimizing lithium-ion batteries for electric vehicle applications and decarbonizing road transport is the ionic and electronic transport in the composite positive electrode. This study presents the use of broadband dielectric spectroscopy (BDS) with frequencies ranging from a few Hz to several GHz to provide a multiscale description of the electronic and ionic properties of two EV-grade battery active materials: $LiNi_{0.5}Mn_{0.3}Co_{0.2}O_2$ (NMC532) and $LiNi_{0.8}Mn_{0.1}Co_{0.1}O_2$ (NMC811), by measuring the permittivity and conductivity as well as the different dielectric relaxations resulting for interfacial space-charges and ionic motions. Dry measurements were obtained using an electrode mix with varying amounts of active material, binder (PVdF-HFP, poly-vinylidene fluoride-co-hexafluoropropylene, and additive conductive agent (carbon black). 1M $LiPF_6$ solution in an ethylene carbonate/diethyl carbonate mixture (EC/DEC 1:1 v/v) was used as electrolyte for wet electrode measurements and ionic observations. The obtained results showed higher electronic conductivity in NMC811, lower electronic percolation threshold of conductive additive, and lower ionic and electronic activation barrier, projecting a better rate performance and higher energy density for the nickel-rich electrode.

Keywords: Lithium-ion battery, permittivity, dielectric, electronic conductivity, ionic conductivity.

Résumé

L'un des défis majeurs dans l'optimisation des batteries lithium-ion pour application aux véhicules électriques et la décarbonation du transport routier est une meilleure compréhension des phénomènes conduisant à une limitation du transport ionique et électronique au sein de l'électrode positive. Cette étude présente la mise en œuvre de la spectroscopie diélectrique large bande (BDS) utilisant des fréquences allant de quelques Hz à plusieurs GHz pour fournir une description multi-échelle des propriétés électroniques et ioniques de deux matériaux actifs de batteries utilisées dans les véhicules électriques : $LiNi_{0.5}Mn_{0.3}Co_{0.2}O_2$ (NMC532) et $LiNi_{0.8}Mn_{0.1}Co_{0.1}O_2$ (NMC811), en correspondantes, résultant des charges d'espace interfaciales et des mouvements ioniques. Les mesures à sec ont été obtenues en utilisant différentes électrodes présentant des quantités variables de matière active, de liant (PVdF, poly-vinylidene fluoride-co-hexafluoropropylene), et d'additif conducteur (noir de carbone). Une solution de $LiPF_6$ 1M dans un mélange de carbonate d'éthylène/carbonate de diéthyle (EC/DEC 1 :1 v/v) a été utilisée comme électrolyte pour les mesures d'électrodes imprégnées, permettant de caractériser les mouvements ioniques. Les résultats obtenus ont montré une conductivité électronique plus élevée dans le cas du NMC811, un seuil de percolation électronique plus bas du noir de carbone, et une barrière d'activation ionique et électronique plus basse, conduisant à de meilleures performances et une densité d'énergie plus élevée pour l'électrode riche en nickel.

Mots-clés : Batterie lithium-ion, permittivité, diélectrique, conductivité électronique, conductivité ionique.

Abbreviations

AM	–	active material
BDS	–	broadband dielectric spectroscopy
CB	–	carbon black
EDS	–	energy-dispersive x-ray spectroscopy
EIS	–	electrochemical impedance spectroscopy
EV	–	electric vehicle
e^-	–	electron
LCO	–	$LiCoO_2$
LFP	–	$LiFePO_4$
LIB	–	lithium-ion battery
LP40	–	1M $LiPF_6$ solution in an ethylene carbonate/diethyl carbonate mixture (EC/DEC 1:1 v/v)
m	–	Archie's exponent
NMC	–	$LiNi_xMn_yCo_{1-x-y}O_2$
NMC532	–	$LiNi_{0.5}Mn_{0.3}Co_{0.2}O_2$
NMC811	–	$LiNi_{0.8}Mn_{0.1}Co_{0.1}O_2$
PVdF-HFP	–	poly-vinylidene fluoride-co-hexafluoropropylene
SEM	–	scanning electron microscopy
TM	–	transition metal
XRD	–	x-ray diffraction
ε	–	permittivity
$\Delta\varepsilon$	–	dielectric strength
ρ_n	–	electronic resistivity
σ_e	–	electronic conductivity
σ_i	–	ionic conductivity
ϕ	–	porosity fraction

1 Introduction

1.1 Background

In an electrochemical cell, energy can be stored as chemical energy and converted into electrical energy to power various devices and equipment when needed[1]. A battery comprises several electrochemical cells connected in series and/or parallel to give the required voltage and capacity[2]. In most applications, the ability to recharge the cells (secondary cells) is preferred to the non-rechargeable cells (primary cells). Hence, the secondary cell design requires energy-delivering chemical reactions, which can be reversed by supplying electrical current in the opposite direction[1].

The transportation sector accounts for about 16.2% of global greenhouse gas emissions, and decarbonizing road transport is projected to cut emissions by about 12%[3]. This can be achieved by developing and optimizing advanced energy storage devices to eliminate tailpipe emissions and overcome the intermittency challenges of wind and solar sources[4]. When compared to other battery systems, lithium-ion batteries (LIBs) are currently the most versatile and efficient option for eco-friendly electric vehicle applications[4,5]. This is due to their performance characteristics, which include higher energy and power density, long cycle life, rapid charge capabilities, and low self-discharge rate[6]. As a result, LIBs have dominated consumer electronics and mobile device applications[6,7].

1.2 Lithium-ion Batteries

Lithium-ion batteries depend on the ability of layered and structured transition metal compounds to undergo reversible intercalation of lithium ions in an electron-transfer process[8]. A lithium-ion cell consists of a positive electrode, a negative electrode, electrolyte, separator, and current collectors (Figure 1). During charging, the electrolyte facilitates the transport of lithium ions from the positive electrode to the negative electrode, where they are stored by intercalation, and electrons leave the positive electrode to the negative one through the current collectors and external circuit. The reverse mechanism occurs during discharge, the positive electrode is re-lithiated, and electrons flow to it, powering an external device. The separator allows only the passage of lithium ions, thereby preventing a short-circuit[6]. The electrochemical reactions are shown in Table 1.

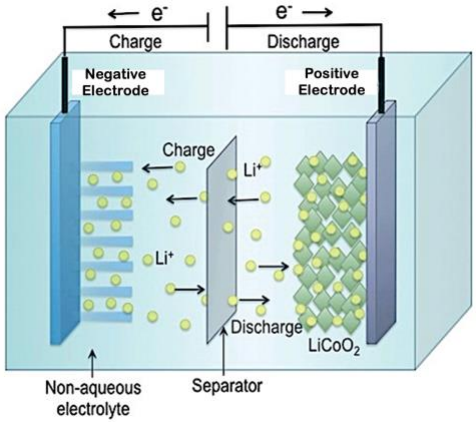

Figure 1. Schematic of electrochemical reactions in a lithium-ion cell.[9]

Table 1. Electrochemical reactions in lithium-ion batteries*.[1]

Positive electrode:	$LiCoO_2 \underset{Discharge}{\overset{Charge}{\rightleftharpoons}} Li_{1-x}CoO_2 + xLi^+ + xe^-$
Negative electrode:	$C + xLi^+ + xe^- \underset{Discharge}{\overset{Charge}{\rightleftharpoons}} Li_xC$
Overall reaction:	$LiCoO_2 + C \underset{Discharge}{\overset{Charge}{\rightleftharpoons}} Li_{1-x}CoO_2 + Li_xC$

* for a Co-based positive and C-based negative electrodes.

The positive electrode in a commercial lithium-ion cell consists of aggregates of electrochemically-active material, a conductive additive (mostly carbon black), and a polymeric binder to ensure composite durability, homogeneously mixed and coated onto a current collector (Figure 2). The negative electrode used is mostly highly-intercalating graphite; hence, the positive electrode material and composition variation are more relevant for power performance and cost optimizations of the battery.

The composite nature of the positive electrode gives rise to several interfaces, including a macroscopic interface between the electrode material and the current collector; mesostructural interfaces (micrometric) between clusters (aggregates of particles) of active materials; and nanometric level interfaces between active material particles and carbon black additive[10]. The liquid electrolyte occupies the defined porosity, creating additional solid-electrolyte interfaces. These interfaces create a compounding limitation to charge depletion and influence the conduction of lithium ions and electrons through the electrode. These interfacial processes and overall cell performance can be influenced by changing parameters such as the nature and amount of active and non-active materials, the size distribution, porosity, electrode thickness, nature of the electrolyte, etc.

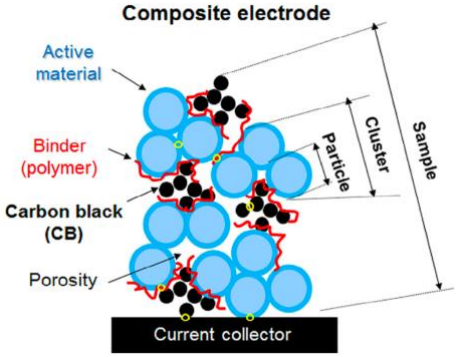

Figure 2. Composite architecture of the positive electrode.[10]

Lithium metal oxides or lithium metal phosphates are used as positive electrode active materials in commercial lithium-ion batteries[6]. $LiCoO_2$ (LCO) has a capacity of 155mAh/g, a nominal voltage of 3.9 V, and good electrochemical performance. However, its high-cost cobalt demands call for other active material configurations for applications in electric vehicles[6]. The high phosphate stability in $LiFePO_4$ (LFP) batteries ensures better safety and a reduced risk of thermal runaway. LFP batteries are also less expensive, with a specific capacity of 160 mAh/g and a voltage of 3.40 V[6]. The most commercialized electrode types are $LiNi_xMn_yCo_{1-x-y}O_2$ (NMC) with varying

amounts of transition metals nickel, manganese, and cobalt and are capable of initial capacity greater than 200 mAh/g[6]. NMCs are made by partly substituting Co in $LiCoO_2$ with Ni and Mn to achieve improved electrochemical performance while reducing the material cost. High discharge capacity is demonstrated in Ni-rich compositions; Mn-rich compositions maintain better cycle life and thermal safety; Co-rich compositions provide excellent rate capability, allowing composition modifications to achieve the desired behavior[5]. The multivalence states Ni^{2+}/Ni^{3+} and Co^{2+}/Co^{3+}, and their occupation fractions determine the performance properties of the NMC composition. Figure 3 summarizes the effect of these composition variations on thermal stability, discharge capacity, and capacity retention[11].

There is increasing interest in Ni-rich electrodes for EV applications due to increased specific capacity, electronic conductivity, and low cost[12]. With increasing nickel content, Wang et al. (2018) reported a broadening of the $Ni^{3+/4+}$ *eg** band, lowering the Fermi level, and decreasing electronic activation energy[13]. However, due to Ni mixing with Li sites, nickel-rich cathodes suffer structural degradation during cycles[5,12].

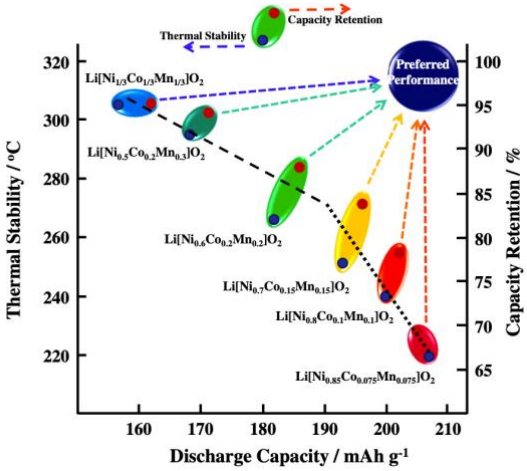

Figure 3. Relationship between thermal stability, discharge capacity, and capacity retention of different NMC compositions.[11]

1.3 Challenges of Lithium-ion Batteries

The major challenges in developing lithium-based rechargeable batteries for electric vehicles include improving safety, increasing energy density by increasing the capacity of reversible lithiation, improving the power density, allowing fast charge/discharge cycles while optimizing for low-cost, environmentally friendly materials, and good chemical compatibility to reduce battery ageing and promote long service life[14]. Unlike the thermodynamic properties, like specific capacity and energy density, the kinetic behavior of NMCs, specifically the power/rate capability, which is primarily determined by the electronic and ionic transport processes, is still poorly understood and crucial for designing high-performance lithium-ion batteries[13].

The target metrics for efficient lithium-ion battery technology in EV applications (Figure 4) reveal the areas where improvements are needed and the minimum goals to be attained[15]. NMC-based lithium-ion batteries currently cover the largest area in the metric chart in terms of specific energy and power, and recent developments have reduced irreversible capacity loss and enhanced the rate capabilities[6].

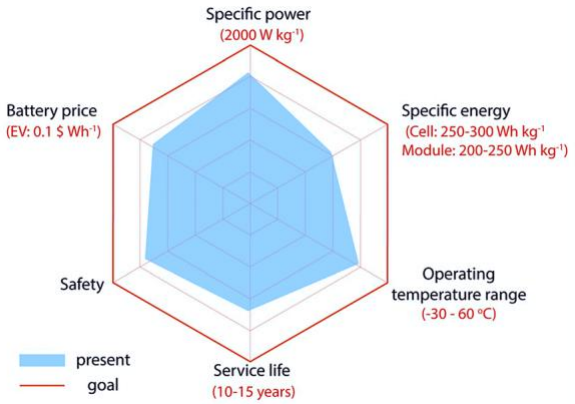

Figure 4. Important target metrics for lithium-ion batteries in electric vehicles.[15]

The cost of lithium-ion batteries has dropped significantly in recent years, with a market average of $137 per kWh, and is expected to go below $100 per kWh by 2023[16]. According to Baker McKenzie's 2022 report, the global manufacturing capacity of lithium-ion batteries has expanded from 14 GWh in 2010 to 457 GWh in 2020, and it is predicted to exceed 2,000 GWh in 2028 due to increasing legislation favoring the production of battery-powered electric vehicles[16].

1.4 Electronic and Ionic Limitations in Lithium-ion Batteries

To close the gap between the theoretical and actual rate performance capabilities of lithium-ion batteries, improvements in the materials, electronic and ionic conductivities are required[17]. However, there is limited literature on the interplay between electrode composition, transport limitations, and electrochemical performance of the battery[18]. Increasing the percentage of conductive additive and reducing the porosity results in higher electronic conductivity. However, electrodes with less porosity have intrinsically slower ion transport, which poses a limitation[17]. The convolution of electronic and ionic conduction processes is typically hard to distinguish[13].

Several studies combine electrochemical impedance spectroscopy (EIS) and direct-current (DC) polarization methods to evaluate ionic and electronic conduction in battery cells. These methods allow for studying charge transfer at the macroscopic interface, ionic diffusion during cycling, and the overall conductivity[17,19]. In a study by Wang et al. (2018), a combination of EIS with DC polarization methods was used to separately measure ionic (σ_i) and electronic (σ_e) conductivities of $LiCoO_2$ and NMCs[13]. With increasing Ni content, they observed a significant increase in both σ_i and σ_e, accompanied by considerable reductions in the activation barriers, accounting for the improved rate capability of the nickel-rich NMCs[13]. Noh et al. (2013) also established a strong correlation between high rate capability, electronic conductivity, and chemical Li diffusivity in several NMCs[11]. A different study combined experiments and modeling to explore the relationship between rate capability and microstructure in a LIB porous electrode[18]. They demonstrated that the porosity of the carbon-binder domain was a vital parameter in obtaining the ionic and electronic percolation network and obtained a threshold value for NMC loading (92 wt.%) over which the electronic transport limitations dominate the rate performance of the electrode[18].

However, a more fundamental understanding of interfacial and rate mechanisms is required[10]. The proposed approach, Broadband dielectric spectroscopy (BDS), involves identifying limiting phenomena by multiscale decomposition studies of the hierarchical electrodes and correlation with the electrochemical performance of the cells[20].

1.5 Broadband Dielectric Spectroscopy (BDS)

Broadband dielectric spectroscopy (BDS) classically studies the movement of ions and dipoles in the presence of an electric field[21]. This technique replaces the light source with an oscillating voltage, and matter interaction is determined by the perturbation of the field[21]. BDS investigates the relaxation and rotation of dipoles at frequencies below 10^{12} Hz (Figure 5), and the frequency at which a particular dipole responds is related to the "relaxation time" of that system (Figure 6a).[10,21]

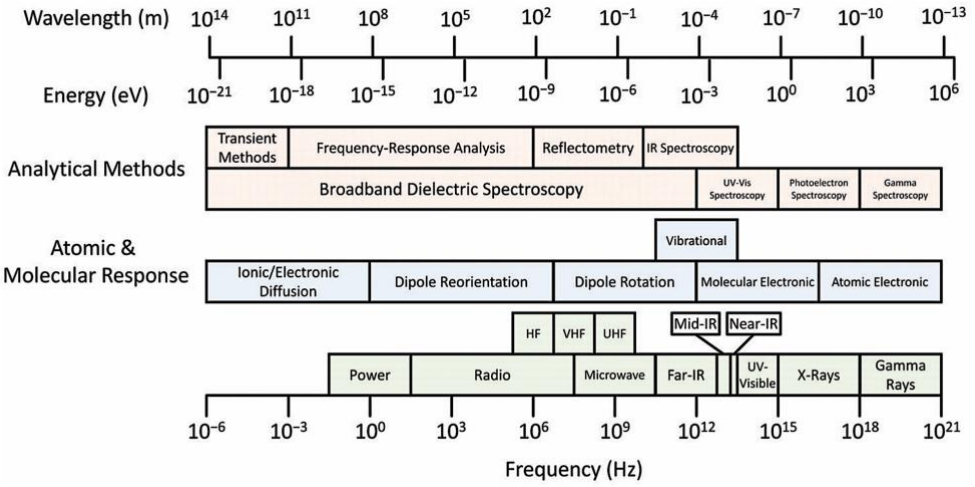

Figure 5. Electromagnetic spectrum with wavelength, frequency, and energy with common spectroscopic techniques listed.[21]

Broadband Dielectric Spectroscopy (BDS) may also be used to describe the electronic transport in electrode materials for lithium batteries by subjecting it to a time-dependent electric field, which can be described by the time-dependent polarization(s) and relaxation(s)[22]. In electronic conductors, several polarization mechanisms occur at different scales (from interatomic to macroscopic sizes) with distinct characteristic frequencies. The smaller scales respond at higher frequencies, and the macroscopic scale has its response at lower frequencies due to the time scale of its polarization (Figure 6b)[10]. The response is expressed by frequency-dependent complex conductivity $\sigma(\omega)$, resistivity $\rho(\omega)$, and relative permittivity $\varepsilon(\omega)$, given by equation (1) where $\varepsilon_0 = 8.84 \times 10^{-12}$ F·m^{-1} is the vacuum permittivity[23].

$$\sigma(\omega) = \rho(\omega)^{-1} = i\omega\varepsilon_0\varepsilon(\omega) \qquad (1)$$

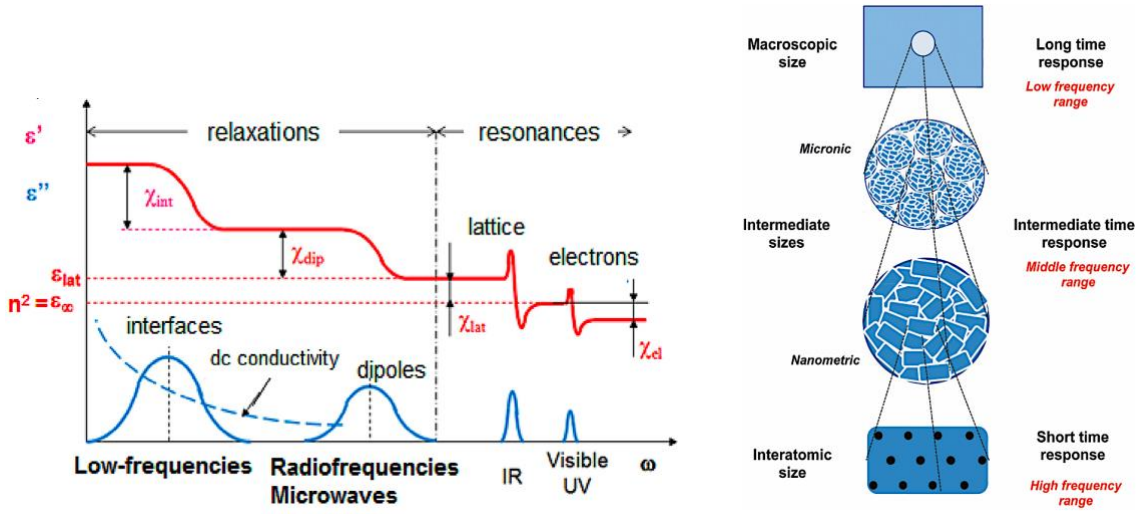

Figure 6. (a) Schematic representation of the real (ε') and imaginary (ε") parts of the permittivity vs. frequency for a solid. (b) Schematic description of a hierarchical architecture at different scales of a powdered material: different sources of polarization vs. frequency and size.[10]

A decomposition procedure of the Nyquist plots of complex permittivity (ε'' vs. ε'), resistivity (ρ'' vs. ρ'), and conductivity (σ'' vs. σ') is used to evidence the different relaxations. The frequency-dependent permittivity of a conducting material is generally given by equation (2)[23].

$$\varepsilon(\omega) = \varepsilon_\infty + \left[\sum_m \frac{\varepsilon_{mL} - \varepsilon_{mH}}{(1 + (i\omega\tau_m)^{1-\alpha_m})^{\beta_m}}\right] + A(i\omega)^{s-1} + \frac{\sigma_{dc}}{i\omega\varepsilon_0} \qquad (2)$$

Where ε_∞ is the residual permittivity, $\omega = 2\pi\nu$ is the angular frequency in rads^{-1} (ν being the frequency expressed in Hz). For each relaxation, ε_{mL} and ε_{mH} are the low and high-frequency limits of the permittivity ($\Delta\varepsilon_m$ is the dielectric strength), τ_m is the mean relaxation time; A, α_m, and β_m are fitting parameters[10]. The term in brackets corresponds to the sum of the m relaxation functions described by the empirical Havriliak–Negami (HN) functions[24] because electrical polarizations at different scales are additive due to their vector character. The relaxation functions that fit most experimental spectra are Debye ($\alpha_m = 0$, $\beta_m = 1$) and Cole–Cole ($\alpha_m \neq 0$, $\beta_m = 1$) functions whose Nyquist representations display arcs of a circle centered on the real axis for the first one and below this axis for the second one[23]. The term $A(i\omega)^{s-1}$ ($0 \leq s \leq 1$), whose contribution occurs in the low-frequency range, is due to a more or less disorderly conductive network (at a macroscopic scale). It can also be due to distributions of contact resistances and capacitance between the metallization and the sample. The Nyquist plot of such behavior is a straight line merged with the sample dc conductivity contribution $\sigma_{dc}/i\omega\varepsilon_0$[23]. The decomposition of the dielectric spectra into several contributions (DC conductivity and relaxations) is carried out by successive subtractions of the contributions starting from the lowest frequencies to the highest ones[23].

In the investigation of the electrical conductivity of a composite electrode, several types of polarizations involving dielectric relaxations appear from low to high frequencies. Polarization of space-charge due to the sample/current collector interface; polarization of aggregates (or clusters) and particles due to resistive junctions; and electron transfers at nanometric or interatomic scale[10]. BDS is a unique technique for these interfacial phenomena, allowing complex permittivity and conductivity measurements over a wide frequency range from 10 Hz to 18 GHz and with temperature variations[23]. The first detailed study of the technique in NMC ($LiNi_{1/3}Mn_{1/3}Co_{1/3}O2$) observed that the main limiting factor of NMC conductivity lies at the junctions between the particles within the various clusters. The charge carriers are highly obstructed at this level, resulting in a conductivity loss of about 3 to 4 orders of magnitude[22].

1.6 Objectives of the study

This study aims to better describe the charge transport in commercial lithium-ion battery electrodes. This will be achieved by studying several electrodes and changing parameters such as the type and composition of active and non-active materials and linking the BDS measurements: ex-situ (dry and wet electrodes), in-situ (electrode in a full cell), and operando (cycling electrode) to the electrochemical performance of the cell. In-situ and operando experiments are not reported in this study but are essential to the overall goal and will be carried out in upcoming experiments. Identifying and discriminating the multiscale electronic and ionic contributions will help optimize battery materials for high capacity and power applications such as electric vehicles.

2 Materials and Methods

2.1 Materials

The NMC powders used in this study were industrially supplied EV battery-grade active material powders; $LiNi_{0.5}Mn_{0.3}Co_{0.2}O_2$ (NMC532) and $LiNi_{0.8}Mn_{0.1}Co_{0.1}O_2$ (NMC811). Other materials used include poly-vinylidene fluoride-co-hexafluoropropylene (PVdF-HFP) (as the polymeric binder), carbon black (TIMCAL SUPER C65) (as conductive additive), acetone (99.8%) (as slurry solvent), 1M $LiPF_6$ solution in an ethylene carbonate/diethyl carbonate mixture (EC/DEC 1:1 v/v) (LP40 as electrolyte), a 3-component mould (7 mm), Hydraulic press, Micrometer screw gauge (± 0.1 µm), Beakers, and a Magnetic stirrer.

2.2 Material Characterizations

2.2.1 XRD Analysis

The x-ray diffraction patterns of the NMC powders were measured with a PANalytical XPert Pro x-ray diffractometer equipped with a Cu $K\alpha_1$ source (λ = 1.5408 Å) operating at 40 kV and 30 mA. The patterns were acquired in a $\theta-2\theta$ configuration with a 2θ range of $10 - 80°$ and a step size of 0.033º.

2.2.2 SEM – EDS Analysis

The surface morphology and cluster size analysis of the electrode materials were obtained by SEM analysis performed using a Zeiss Supra 55 variable-pressure scanning electron microscope with a field emission gun, equipped with an energy-dissipative X-ray detector for chemical microanalysis.

2.3 Sample Preparation

The required amount of PVdF-HFP (binder) was mixed with 20 ml of acetone (99.8%) and stirred for 3 hours in a magnetic stirrer at room temperature. Calculated quantities of NMC and CB to give the needed volumetric percentages were added to the solution and stirred for 15 hours to ensure component homogeneity. The solvent was then evaporated at 50 ºC, and the mixture was ground and vacuum-dried for 2 hours at 90 ºC. The dry electrode material is subsequently stored in a desiccator to avoid interaction with moisture.

Cylindrical pellets were prepared by compacting specific amounts of electrode powder in a 3-component mould (diameter = 7 mm) at 250 MPa. The thickness of the resulting pellet was measured with a micrometer screw gauge, and the pellet was transferred to a sample holder (to prevent an air gap with the instrument). Silver paste was applied to both faces of the cylindrical pellet, as shown in Figure 7, to ensure good metallic contact with the instrument's waveguide (3 mm) and short-circuit (7 mm). The weight and volume percentage of the prepared electrode are shown in Table 2. Sample porosity is determined from each component's density, volume fraction, and the electrode's volume.

Table 2. Weight and Volume percentage of prepared electrodes.

Samples	**Weight %**			**Volume %**			
	NMC AM	PVdF-HFP	CB	NMC AM	PVdF-HFP	CB	Porosity
A	97.5	2.5	0	67.5	4.5	0	28
B	95.5	2.0	2.5	64.5	3.5	4.0	28
C	93.5	3.0	3.5	61.5	5.2	5.3	28
D	91.5	4.0	4.5	58.2	6.8	7.0	28

2.4 BDS Measurement

The BDS setup (Figure 7) consists of a cylindrical electrode sample of known composition and dimension with silver paint on both faces placed in a disk-shaped sample holder, at the discontinuity of the coaxial waveguide in an ex-situ cell, connected to a Keysight 4990 low-frequency impedance analyzer and an Agilent E8364B high-frequency network analyzer. A tight sealing and a counter electrode are included for in-situ and operando measurements (with electrolyte). In this study, however, due to technical constraints, electrodes wetted with electrolyte were used in an ex-situ cell to observe the ionic contributions.

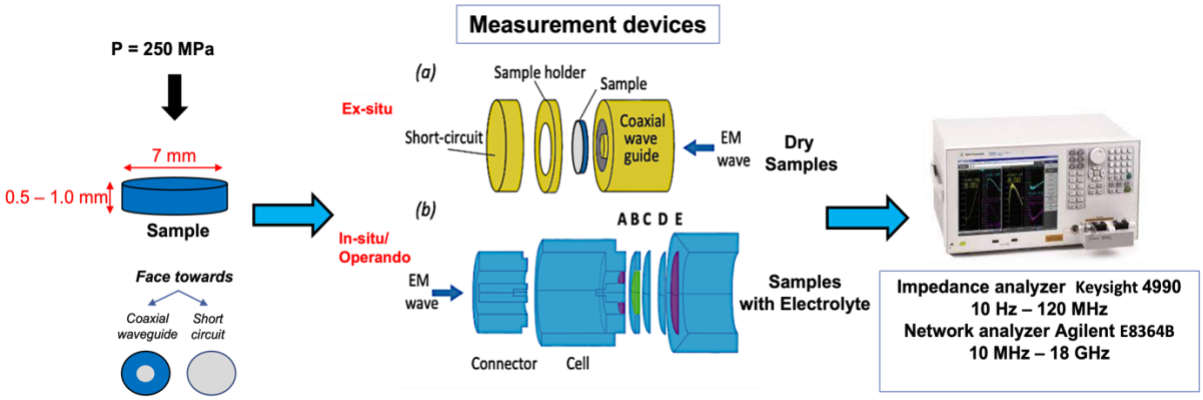

Figure 7. BDS Setup. L*eft:* Cylindrical electrode sample dimension and silver metallization. C*enter:* Measurement devices (a) Ex-situ cell (b) In-situ/Operando cell; **A**: sealing (tight glass window) B: sample and sample holder **C**: short-circuit (aluminium grid) **D**: porous glass paper separator **E**: counter-electrode (Li).[20,25]. *Right:* Impedance analyzer.

The electromagnetic wave admittance of the sample was measured over multiple frequency bands, with a frequency overlap ranging between 50 – 120 MHz in the two analyzers, confirming the agreement of the measurement[23]. The frequency limitation of the setup is the theoretical cut-off frequency of 19.6 GHz for the standard "APC7" used in the "SuperMit cell "[26]. An excitation port at the input of the coaxial line enables the generation of an incident transverse electromagnetic (TEM) field and, at the same time, absorbs the reflected mode. The complex admittance Y is related to the reflection coefficient at the discontinuity by equation (3). Where Y_0 = 0.02 S (50 Ω) is the characteristic admittance of the coaxial line[27].

$$Y = Y_0 \frac{1 - \Gamma}{1 + \Gamma} = G + jB \qquad (3)$$

A calibration procedure is used to obtain a reference plane to minimize systematic errors generated by the analyzers, waveguides, and dc-block in measurements. The calibration kit includes a 50 Ω impedance load with the reflection coefficient Γ(ω) = 0, an open-circuit with capacitance C = 89 femtofarad (impedance Z = 1/jCω), and a short-circuit with the reflection coefficient Γ(ω) = –1 (and impedance Z = 0)[20].

Following a successful calibration and complex admittance measurement, the permittivity ε(ω) = ε′(ω) − iε″(ω) and conductivity σ(ω) = σ′(ω) − iσ″(ω) of the sample are calculated. The dielectric spectra comprise 402 measuring points, and temperature-varied measurements were obtained using dry nitrogen flux at temperatures between 200 and 300 K.

3 Results and Discussion

3.1 Physico-Chemical Characterizations

3.1.1 X-ray Diffraction (XRD)

The XRD diffraction patterns of active material powders NMC532 and NMC811 are shown in Figure 8a. The two materials show sharp and well-defined diffraction peaks, indicating high crystallinity.

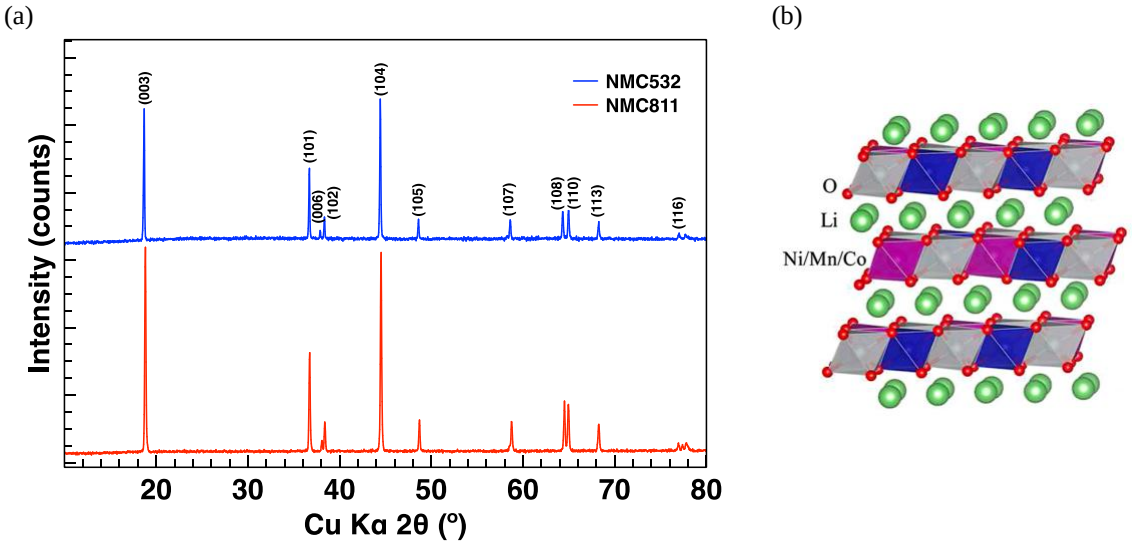

Figure 8. (a) X-ray diffraction patterns of NMC532 and NMC811 active materials, (b) NMC lattice with the $R\bar{3}m$ space group.[5]

The peaks can be indexed to a hexagonal layered structure with space group $R\bar{3}m$ (α-$NaFeO_2$ structure)[13], with lithium (Li), oxygen (O), and transition metals (TM) occupying alternate atomic layers, and the TM located at the center of the oxygen octahedron with same atomic site occupation probability (Figure 8b)[5]. The $R\bar{3}m$ phase can be categorized as hexagonal according to the crystal family, trigonal according to the crystal system, and rhombohedral according to the lattice system[23]. The evident separation of peaks (006) and (102), as well as (108) and (110), indicates a well-defined layered structure[13,23].

3.1.2 Scanning Electron Microscopy (SEM)

The SEM images reveal the morphology and distribution of the active material powder and electrode materials. Both materials are composed of spherical-shaped aggregates (clusters) with a large size distribution. In NMC532 (Figure 9), the average cluster size is 13 ± 4 µm, while in NMC811 (Figure 10), the average size is 10 ± 4 µm. With the addition of binder (PVdF-HFP) and carbon black, there is a nearly homogenous distribution of the CB/binder network throughout the electrode mix. Also, cluster fractures due to electrode compression were observed in the calendered electrodes (Figure 9d).

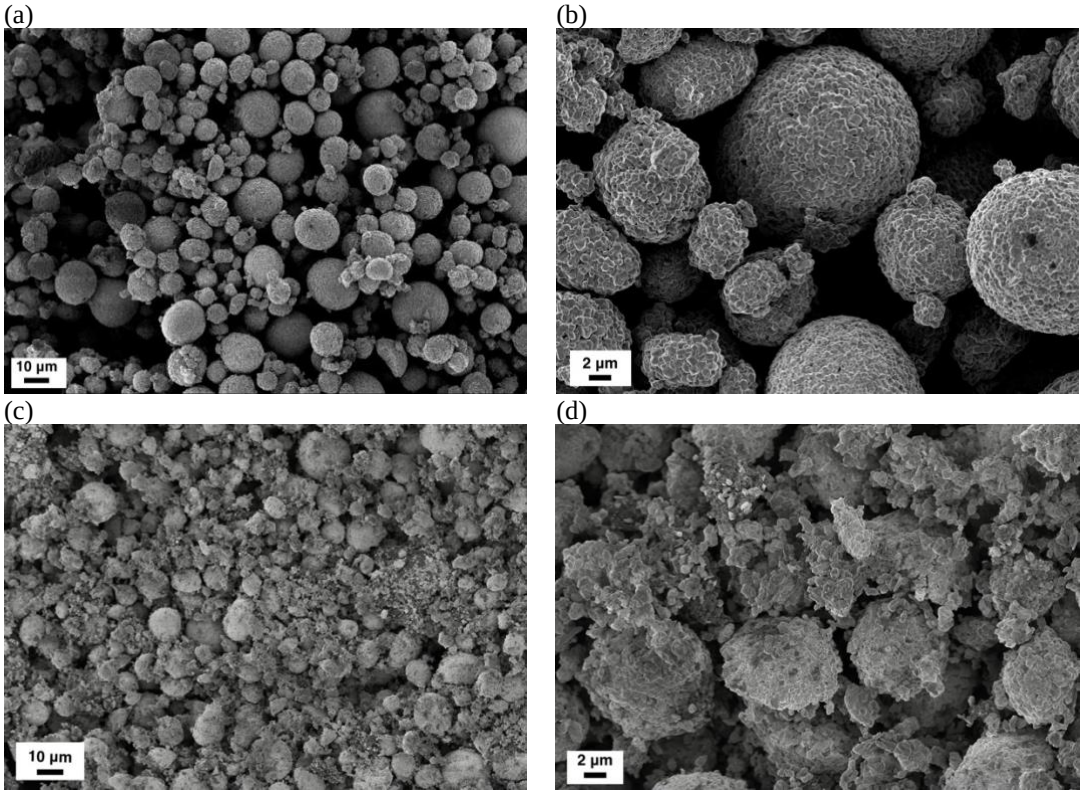

Figure 9. SEM images of NMC532 clusters (a,b), and electrode mix with 5% CB (c,d)

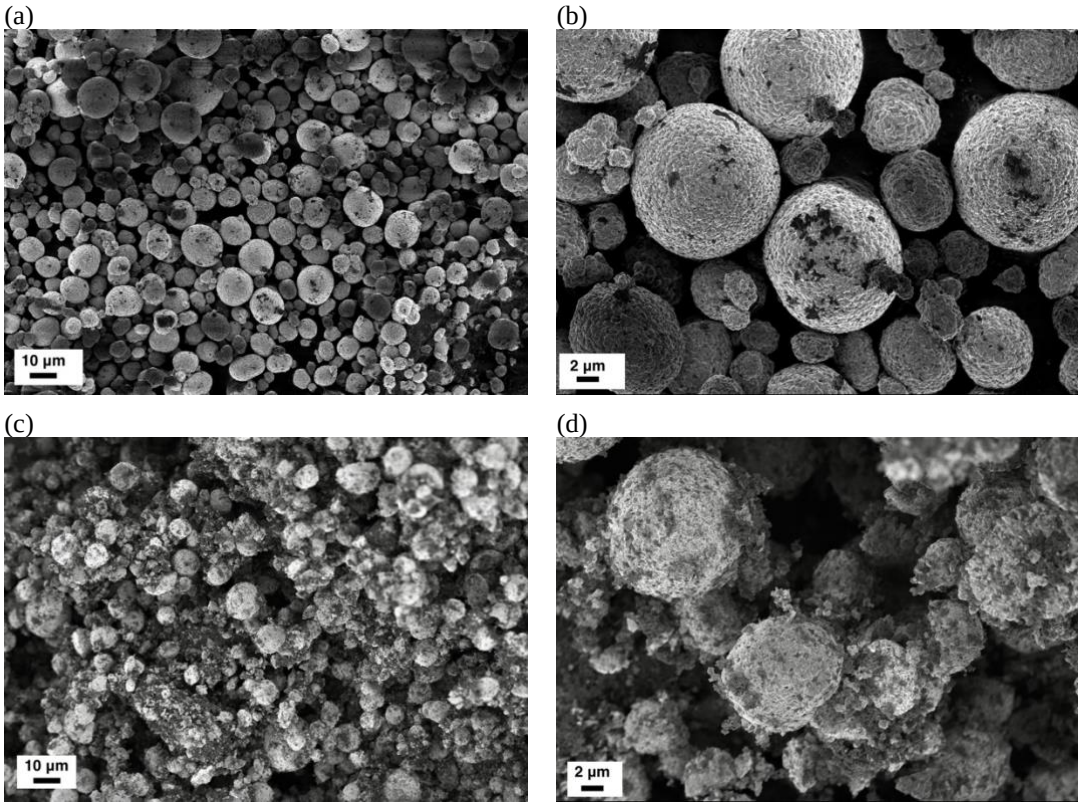

Figure 10. SEM images of NMC811 clusters and particles. (a,b), 5%CB (c,d)

3.1.3 Energy Dispersive Spectroscopy (EDS)

A complementary chemical microanalysis of the active material powders by EDS was used to obtain the chemical stoichiometry of the materials (Figure 11). The obtained sample composition confirms a good agreement with the expected stoichiometry for each active material – with NMC811 having ca. 81% Ni and NMC 532 having ca. 50% (Table 3).

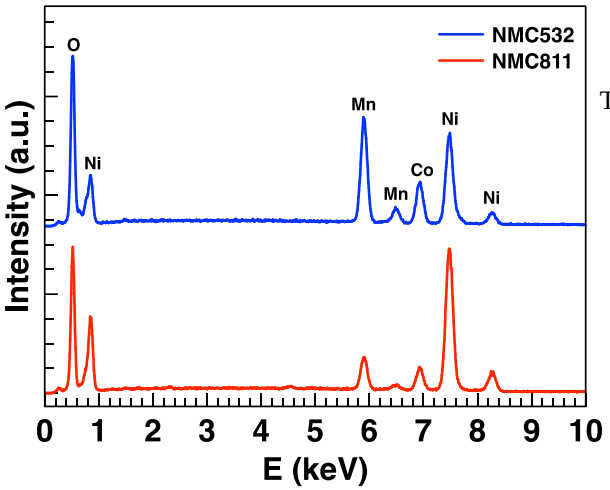

Figure 11. EDS Spectra of NMC532 and NMC811.

Table 3. Percent composition of NMC532 and NMC811 by EDS.

TM	NMC532	NMC811
Ni (%)	49.57	81.23
Mn (%)	30.70	8.79
Co (%)	19.72	9.99

3.2 Broadband Dielectric Spectroscopy (BDS)

The scale-dependent relaxation frequency in a geometrical approach gives smaller-size systems a relaxation response at higher frequencies and the larger scales in the hierarchy at lower frequencies[10]. Additionally, in a kinetic approach, a shift to higher frequency is also observed with increasing density and the mobility of the charge carrier (e.g., ionic contributions are generally observed at lower frequencies than electrons)[10].

3.2.1 Ex-situ Measurements (Dry Electrode)

The evolution of the real parts of permittivity and conductivity with frequency for NMC532 and NMC811 dry electrodes are shown in Figure 12 and Figure 13 respectively. The permittivity decreases as a function of frequency due to scale-lowering and decreasing charge density. The conductivity figures show increased conductivity with frequency due to increasing charge depletion and less contact resistance as it approaches the core active material interfaces. With the introduction of the conductive additive, carbon black (CB), there is a significant increase in the dc-conductivity at a lower frequency (< 10^7 Hz) due to the occupation of CB within the cluster networks and a lowering of contact and space-charge resistances. The dc/sample conductivity saturation is observed at 7% CB for NMC532 and 5% CB for NMC811.

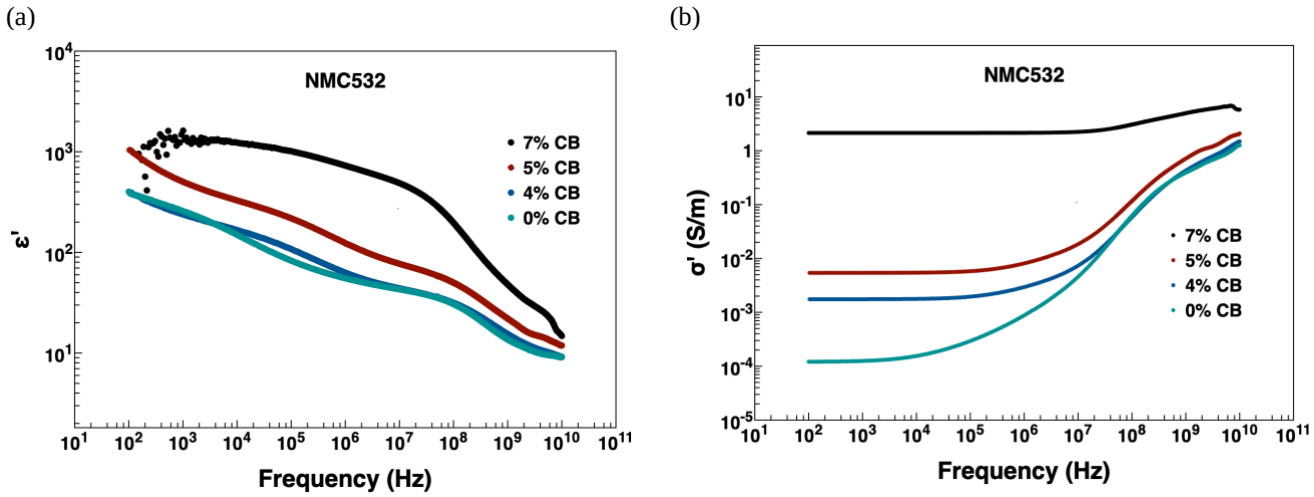

Figure 12. Real parts of (a) permittivity and (b) conductivity as a function of frequency for NMC532 dry electrode with increasing CB vol.%.

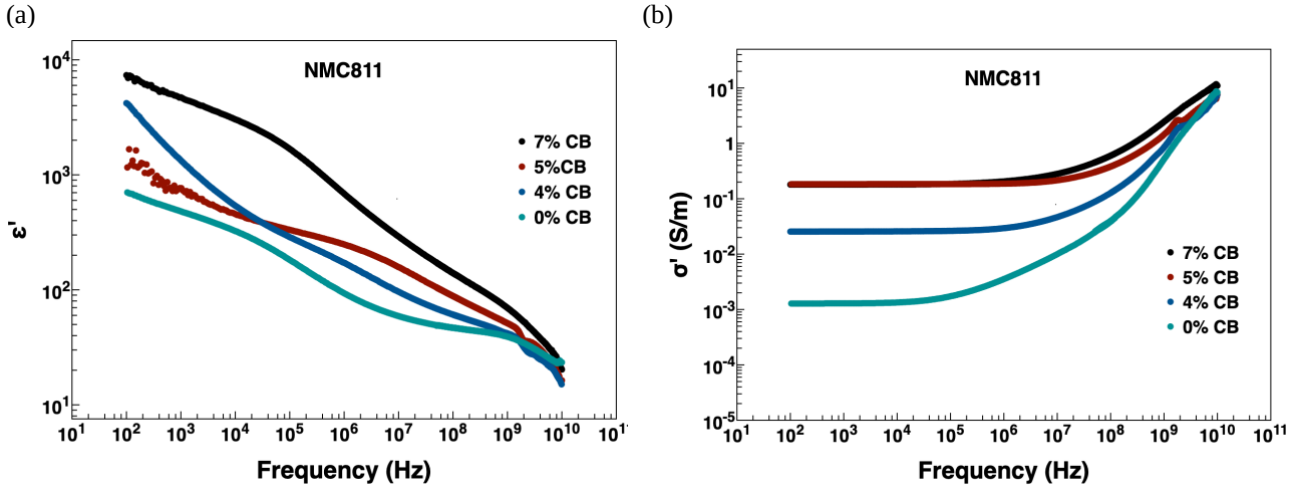

Figure 13. Real parts of (a) permittivity and (b) conductivity as a function of frequency for NMC811 dry electrode with increasing CB vol.%.

The decomposition of the dielectric spectra into several contributions (dc conductivity and relaxations) is carried out by successive subtractions of the contributions starting from the lower frequencies. The low-frequency part of the spectrum is well fitted by a quasi-vertical straight line (P1 contribution) corresponding to the sample dc conductivity (Figure 14a). After subtracting the P1 contribution, the subsequent dielectric relaxations are fitted to the Cole-Cole function (Equation (3). The relaxations P2b, P2, P3, and P4, are thus space-charge relaxations associated with the binder/NMC assembly, sample polarization, active material cluster, and particle polarizations, respectively[23]. From the resistivity Nyquist (Figure 14b), the conductivity values of the sample and cluster are also obtained.

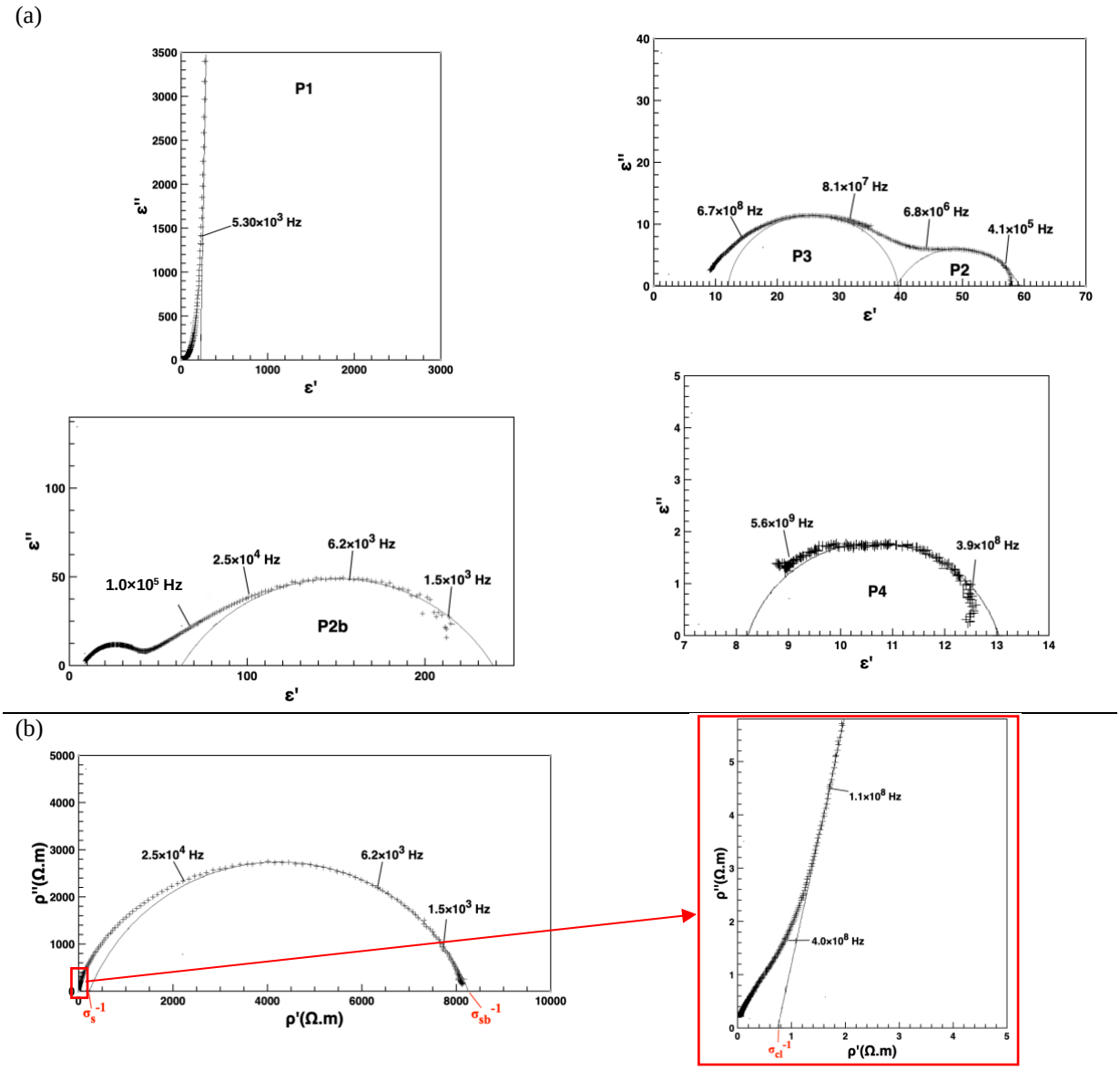

Figure 14. Nyquist plots of (a) complex permittivity, ε′′(ω) vs. ε′(ω) (b) complex resistivity, ρ′′(ω) vs. ρ′(ω) of NMC532 dry electrode, 0% CB at RT (293 K).

The evolution of the dielectric spectra with temperature provides additional information on the thermal activation of the polarizations and conduction mechanisms in the dry electrode. With NMC532 in the absence of CB (Figure 15), the sample has a significant activation barrier at low and high frequencies, evidenced by the lowering of the permittivity and conductivity with decreasing temperature. This thermal activation becomes less significant with increasing CB vol.%, and the near-zero conductivity activation with 7% CB (Figure 16b) represents the behavior of a percolated electrode as the quasi-metallic CB/binder composite becomes the principal electronic pathway[20].

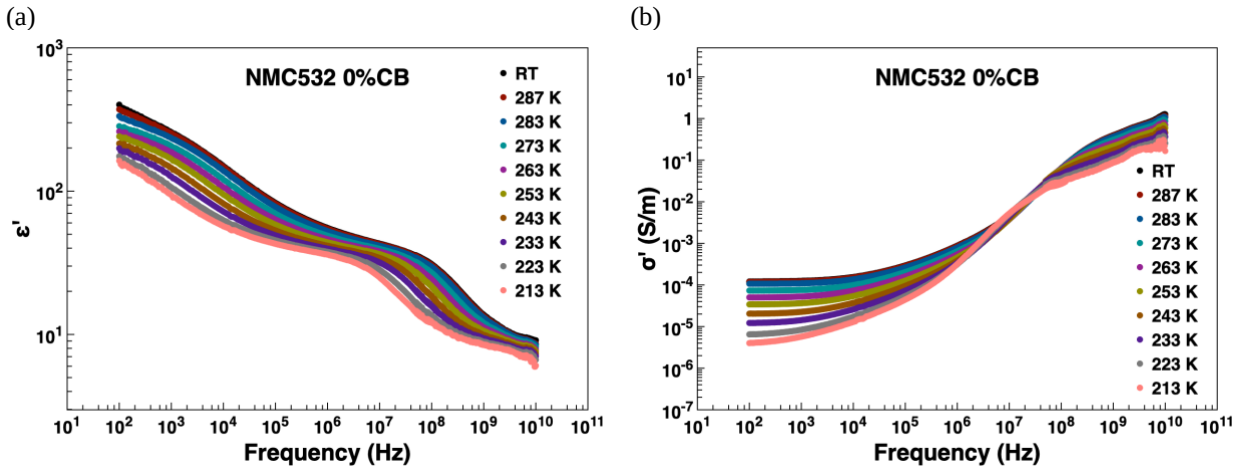

Figure 15. Real parts of (a) permittivity and (b) conductivity as a function of frequency for NMC532 dry electrode 0% CB with temperature varied.

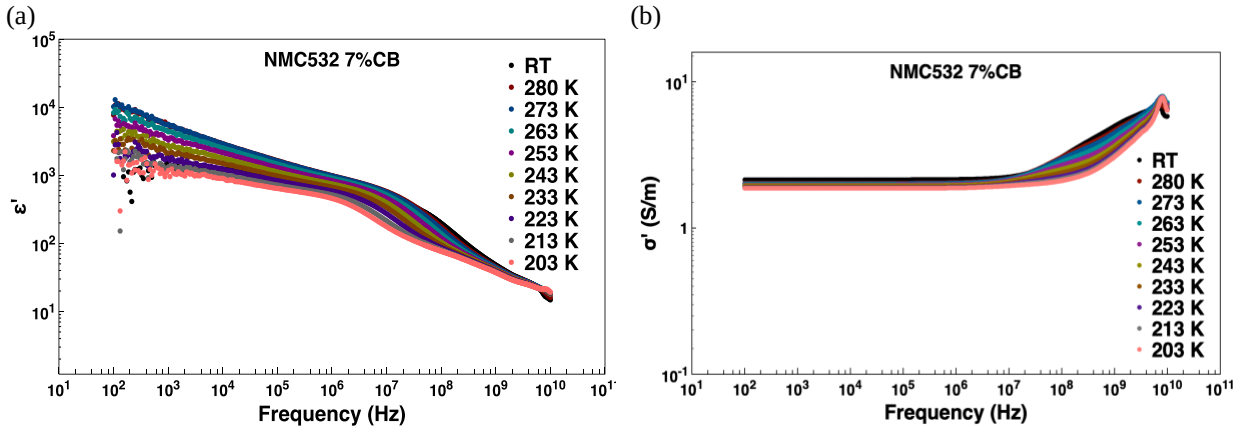

Figure 16. Real parts of (a) permittivity and (b) conductivity as a function of frequency for NMC532 dry electrode 7% CB with temperature varied.

The activation of the relaxation frequencies and conductivity values associated with the various phenomena follows the Arrhenius law (Equation(4)[23], where ν_{0n} and σ_{0n} are the pre-factors; E_n is the activation energy; T is the temperature, and $k = 1.38 \times 10^{-23}$ JK^{-1} is the Boltzmann constant. The resulting Arrhenius plots for NMC532 dry electrode with 0% CB are presented in Figure 17.

$$\nu_n = \nu_{0n}\exp\left(-\frac{E_n}{kT}\right) \qquad \sigma_n = \sigma_{0n}\exp\left(-\frac{E_n}{kT}\right) \qquad (4)$$

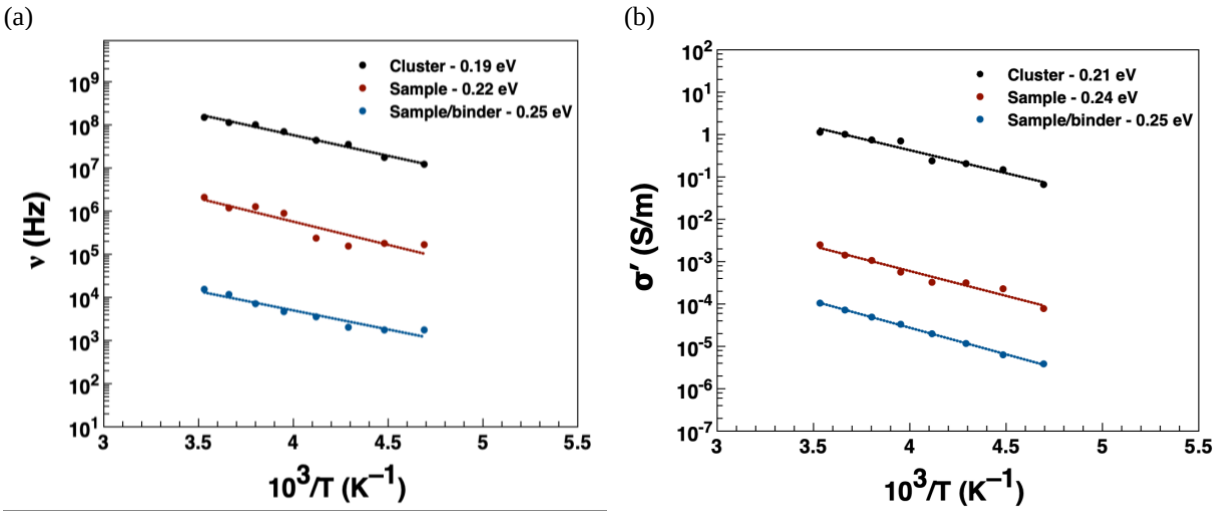

Figure 17. Arrhenius plots of (a) dielectric relaxation frequency (b) real conductivity in the sample/binder, sample for NMC532 dry electrode 0% CB.

A comparison of the obtained parameters and activation energies in NMC532 and NMC811 is presented in Table 4. With scale increase, i.e., from particle to cluster to sample, the activation barrier increases, and the relaxation frequency and conductivity values reduce exponentially. The cluster, sample, and dc conductivity of the nickel-rich NMC811 dry electrode is one order of magnitude higher than NMC532 (p-type semiconductor) and with a lower activation barrier, in agreement with increased electron density in nickel-rich electrodes and NMC811 as an n-type semiconductor; with its Fermi-level closer to the conduction band[5].

The threshold of electronic percolation was also observed at a lower CB vol.% for NMC811 – 4% CB, while it is 5% CB for NMC532, suggesting a possible increase in specific capacity due to less required non-active material.

Table 4. Obtained dielectric parameters for NMC532 and NMC811 dry electrode 0% CB at RT (293 K).

	NMC532	**NMC811**
Sample/binder Conductivity, σ_{sb} (S/m)	1.19×10^{-4}	1.27×10^{-3}
Sample Conductivity, σ_s (S/m)	4.57×10^{-3}	1.81×10^{-2}
Cluster Conductivity, σ_{cl} (S/m)	1.35	1.80×10^{1}
Sample/binder Polarization, ν_{sb} (Hz) E_{sb} (eV)	1.09×10^{4} 0.25	1.26×10^{5} 0.17
Sample Polarization, ν_s (Hz) E_s (eV)	1.26×10^{6} 0.22	4.08×10^{6} 0.19
Cluster Polarization, ν_{cl} (Hz) E_{cl} (eV)	1.55×10^{8} 0.19	3.17×10^{9} 0.16
Particle Polarization, ν_p (Hz) E_p (eV)	1.26×10^{9} 0.16	-

3.2.2 Wet Electrode Measurements

To observe the ionic motion and the influence of adsorbed ions on the electrode conductivity and NMC cluster polarization, liquid electrolyte LP40 (1M $LiPF_6$ solution in an ethylene carbonate/diethyl carbonate mixture 1:1 v/v) was introduced to the compressed electrode to fill in the porous layer. A comparison between the dielectric spectra of the dry and wet electrodes is presented in Figure 18 and Figure 19 for NMC532 and NMC811, respectively.

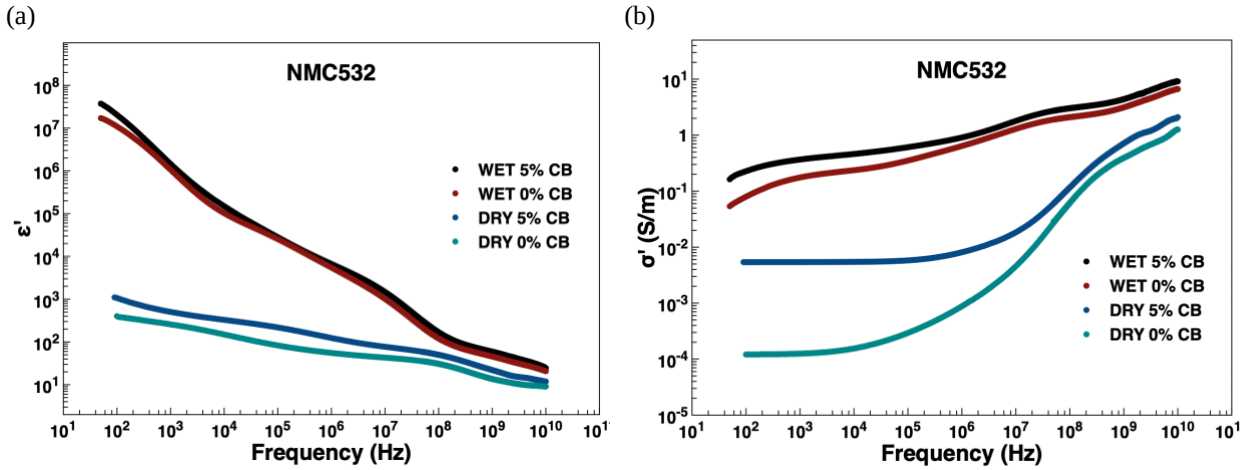

Figure 18. Real parts of (a) permittivity and (b) conductivity as a function of frequency for NMC532 dry and wet electrodes at 0% and 5% CB.

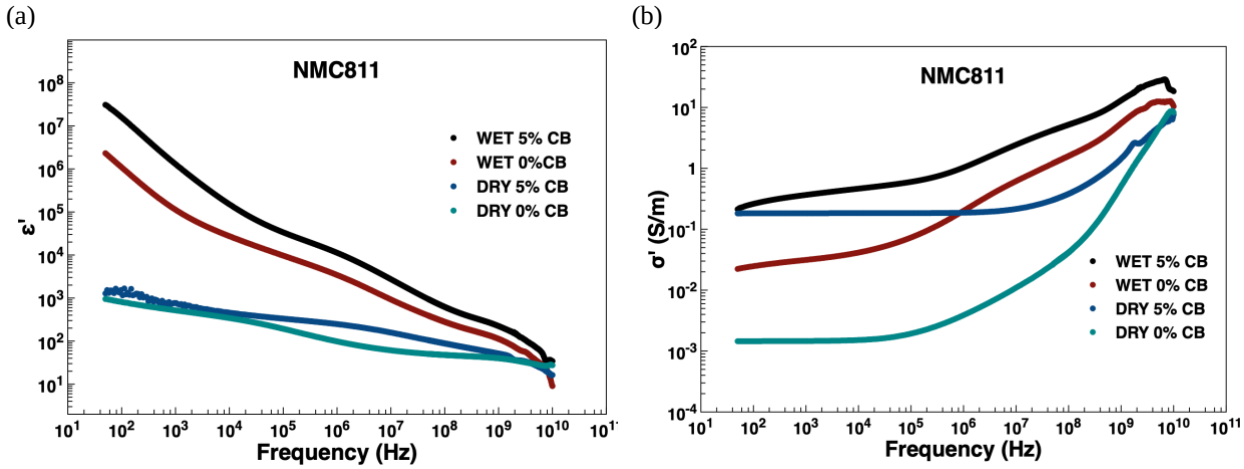

Figure 19. Real parts of (a) permittivity and (b) conductivity as a function of frequency for NMC811 dry and wet electrodes at 0% and 5% CB.

With the introduction of ions, There is a significant increase in the permittivity and conductivity values, especially at lower frequencies, characteristic of the ionic contributions. The influence of CB addition on the conductivity of the wet electrode is also less significant when compared to the dry electrode; this may be due to the lowering of CB conductivity in the presence of the electrolyte[28]. The Nyquist decomposition (Figure 20) reveals five dielectric relaxations with low relaxation frequency W1 associated with the polarization of the ionic double-layer at the sample-electrolyte interface. The W2 relaxation is due to ionic motion and is thermally activated up to the freezing temperature of the electrolyte between 248 and 253 K[28]. The other relaxations, W3, W4, and W5, are associated with the sample, cluster, and particle polarizations, respectively. These

polarizations are associated with a significant increase in dielectric strength Δε, corresponding to the space-charge or double-layer capacity. This increase is a result of the presence of adsorbed ions in the space-charge regions, which greatly decreases the thickness of the space-charge ω (as $\Delta\varepsilon \alpha \omega^{-1}$)[20,23]. The conductivity Nyquists (Figure 20b) is more suitable to observe the effective conductivity contributions as ion and electron flows are carried out in parallel[23].

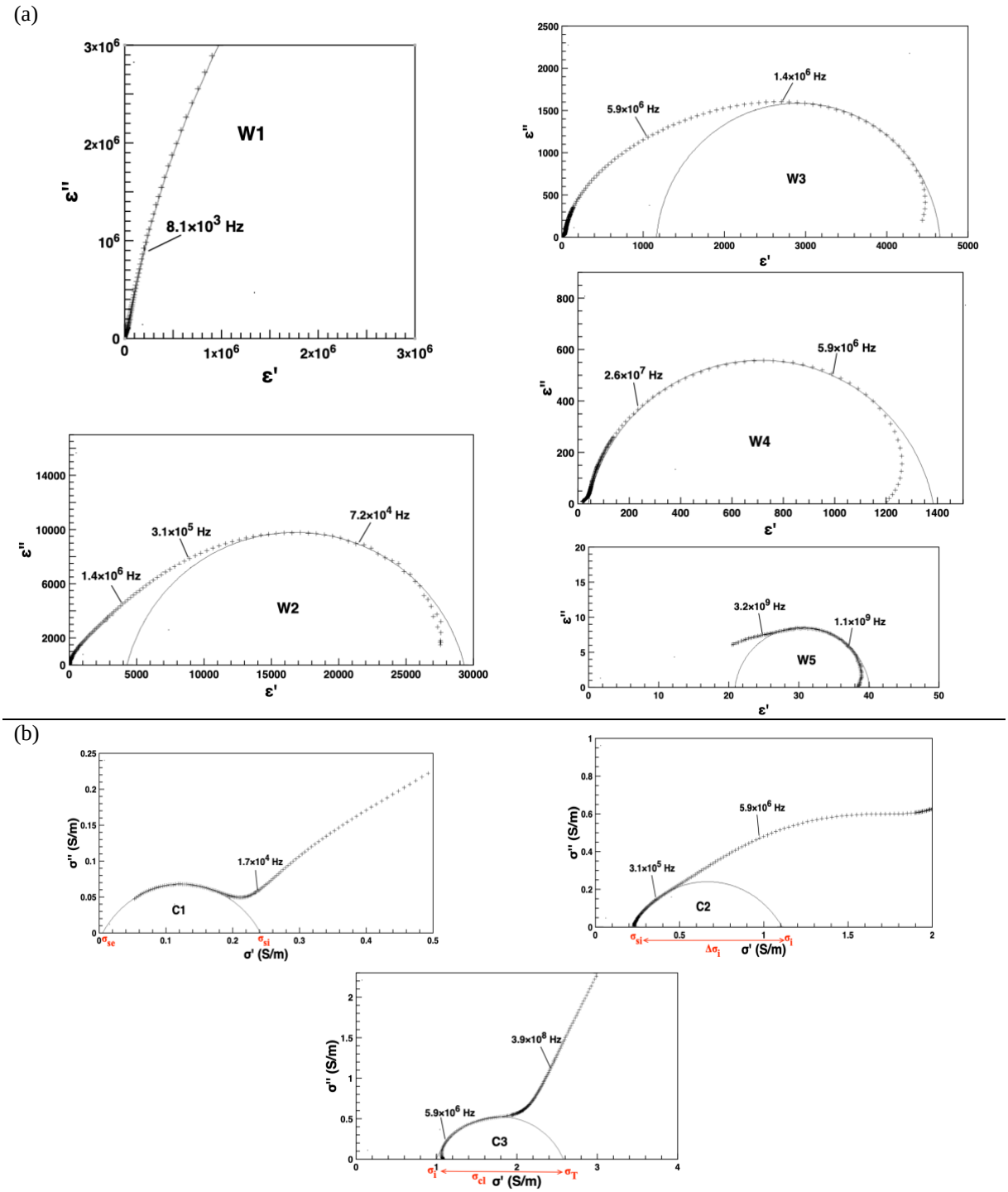

Figure 20. Nyquist plots of (a) complex permittivity, ε′′(ω) vs. ε′(ω) (b) complex conductivity, σ′′(ω) vs. σ′(ω) of NMC532 wet electrode, 0% CB at RT (293 K).

The evolution of the dielectric spectra with temperature (Figure 21) reveals thermal activation across all frequencies. At low frequency (< 10^7 Hz), a significant drop in conductivity and increased activation energy is observed below the freezing point of the electrolyte (< 253 K). The dielectric parameters of the wet electrode also follow the Arrhenius law (4). The effect of electrolyte freezing on the relaxation frequency of ionic motion (Figure 22a) and ionic conductivity (Figure 22b) can be observed as the values drop sharply below freezing temperature.

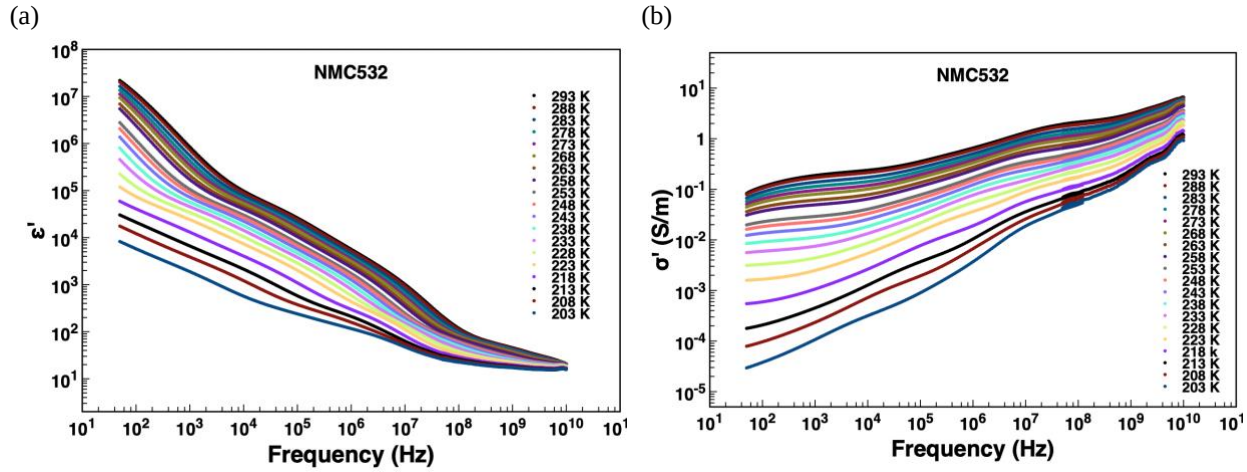

Figure 21. Real parts of (a) permittivity and (b) conductivity as a function of frequency for NMC532 wet electrode 0% CB with temperature varied.

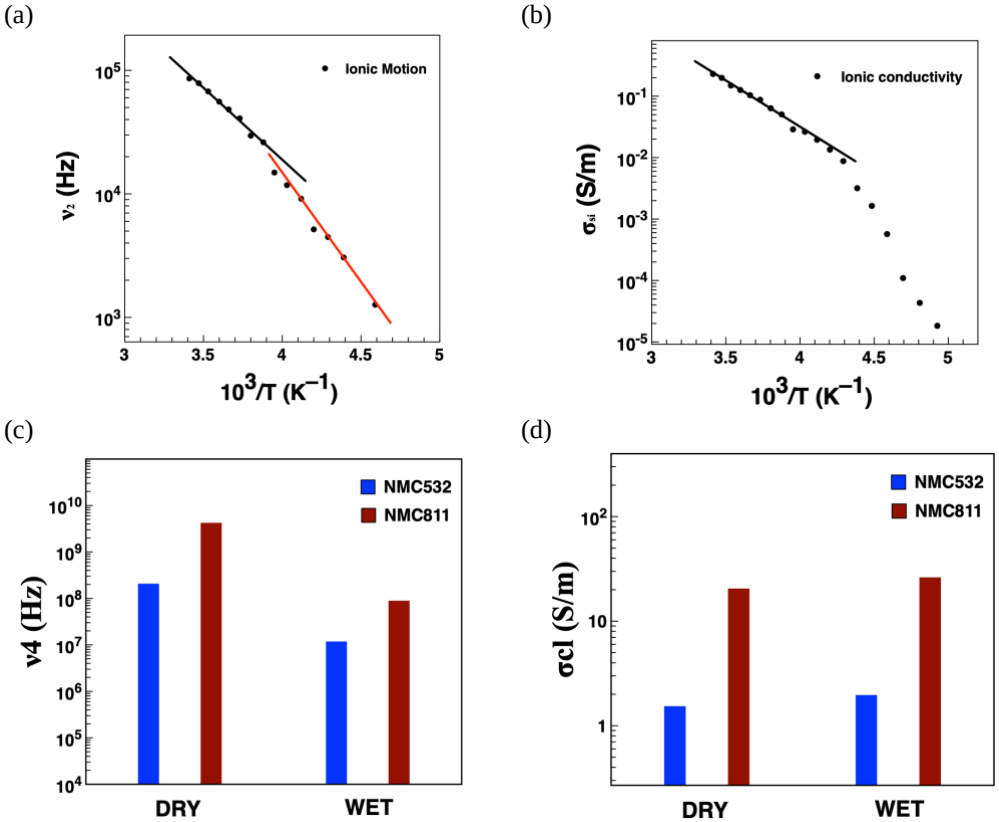

Figure 22. Arrhenius plots of (a) relaxation frequency of the ionic motion ν_2 in NMC532 (b) bulk ionic conductivity σ_{si}. Comparison of NMC532 and NMC811 (c) cluster relaxation frequencies ν_4 (d) cluster conductivity σ_{cl} in dry and wet electrodes at RT.

The lower values of cluster relaxation frequency observed in the wet electrodes (Figure 22c) can be linked to changes in the space-charge depletion layer. The relatively high charge density on the cluster surface increases the time scale of electrical polarization and lowers the relaxation frequency. The conductivity, however, is increased in the wet electrodes (Figure 22c) due to the elimination of cluster surface resistance. Hence, in the wet electrodes, we observe the core conductivity of the cluster[23]. A summary of the obtained dielectric parameters in NMC532 and NMC811 wet electrodes is presented in Table 5.

Table 5. Obtained dielectric parameters for NMC532 and NMC811 wet electrode0% CB at RT (293 K) and the activation energy above freezing temperature.

	NMC532	**NMC811**
Bulk ionic Conductivity, σ_{si} (S/m)	2.43×10^{-1}	3.38×10^{-2}
Local ionic Conductivity, σ_{i} (S/m)	8.64×10^{-1}	7.23×10^{-2}
Cluster Conductivity, σ_{cl} (S/m)	1.72	2.30×10^{1}
Double-layer capacitance, ν_1 (Hz) E_1 (eV)	1.47×10^{2} 0.27	6.85×10^{0} -
Ionic Motion, ν_2 (Hz) E_2 (eV)	1.02×10^{5} 0.23	3.75×10^{4} 0.26
Sample Polarization, ν_3 (Hz) E_3 (eV)	1.14×10^{6} 0.21	7.12×10^{6} 0.19
Cluster Polarization, ν_4 (Hz) E_4 (eV)	8.87×10^{6} 0.21	6.67×10^{7} 0.14
Particle Polarization, ν_5 (Hz) E_5 (eV)	2.45×10^{9} 0.18	1.36×10^{9} -

A set of forward−backward ionic movements describes the long-range conductivity σ_{si} (or bulk ionic conductivity), and the short-range conductivity σ_i (or local ionic conductivity) is linked to hopping between adsorption sites[20,23]. Using Archie's law (5) to relate the liquid electrolyte conductivity σ_{el} and the ionic conductivity σ_{si}, we can estimate the electrode tortuosity, defined as the ratio of the actual distance traveled by the ions per unit length of the medium. The tortuosity is a measure of the lengthening of the transport channel by the twisted structures of the pores in the presence of the solid electrode materials[7,23].

$$\sigma_{\mathrm{si}} = \sigma_{\mathrm{el}} . \phi^{m} \qquad (5)$$

Where ϕ is the porosity volume fraction and the exponent *m* is Archie's exponent, correlated to the tortuosity factor. With σ_{el} = 1 S/m (LP40)[28], and $\phi = 0.28$, the calculated *m* value is 1.1 for NMC532, and 2.7 for NMC811. The *m* value in the NMC811 electrode agrees with that obtained for similar electrodes[23], while its low value in NMC532 may be due to microporosity (additional ionic pathways within the AM clusters).

4 Conclusions and Perspectives

This study presents the multiscale description of ionic and electronic transport in two electric-vehicle grade lithium battery materials; NMC532 and NMC811, using broadband dielectric spectroscopy to provide fundamental and intrinsic details of the ion and electron transport and to gain additional information on how the composite variations influence its properties and ultimately the performance. Figure 23 summarizes the relaxation frequency and energetic barriers (activation energies). NMC811 is generally associated with higher frequency and lower activation energy for each contribution. However, the lower barrier to ionic motion in NMC532 may be due to its microporosity. In addition, the wet NMC811 cluster has a lower relaxation frequency barrier relative to the dry cluster, which implies improved electrical polarization in the presence of the electrolyte. The nickel-rich electrode (NMC811) is therefore projected to have better rate performance.

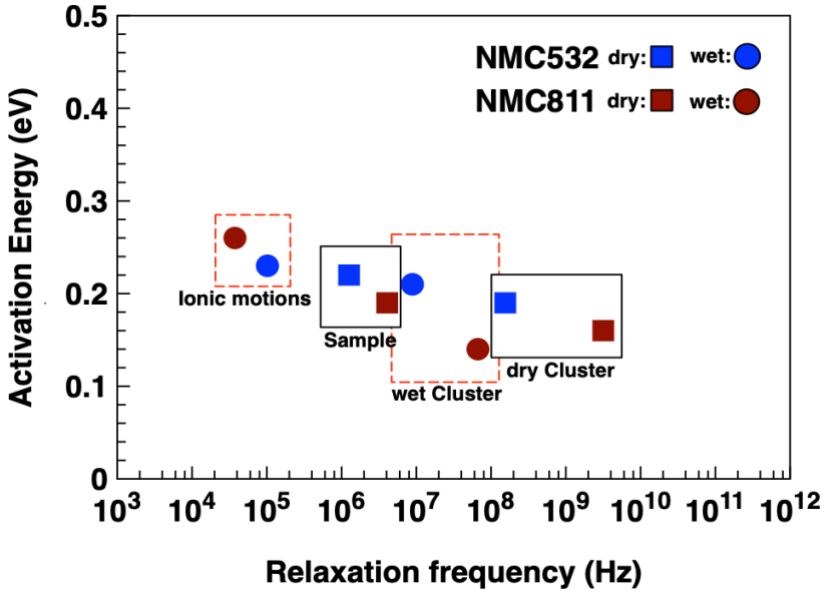

Figure 23. Activation energies vs. relaxation frequencies at RT attributed to ionic motions in the pore network filled with LP40 and electronic motions in the samples and clusters of NMC532 and NMC811 with 0% CB.

As a perspective, it will be essential to correlate these results with the full-cell rate performance by multiple galvanostatic cycling measurements. Further BDS measurements, including full-cell in-situ and operando measurements described in the report, will also be important to characterize the electrode behavior. Other complementary measurements include electrochemical impedance spectroscopy (EIS), to describe the correlation of the low-frequency ionic contributions and macroscopic electronic contributions in the complete cell, and focused ion beam–scanning electron microscopy (FIB-SEM), to provide an improved morphological description from the 3D geometry of the electrode. The results obtained from this study will serve as additional preliminary results in supporting theoretical studies, electrode modeling, and the overall study of transport limitations in composite battery electrodes and material optimizations, especially for electric vehicle applications.

References

1. Kazda, T. & Vanýsek, P. The chalkboard: Lithium batteries as electrochemical sources of energy. *Electrochemical Society Interface* **25**, 47–49 (2016).
2. Tarascon, J.-M. & Armand, M. *Issues and challenges facing rechargeable lithium batteries*. www.nature.com (2001).
3. Emissions by sector - Our World in Data. https://ourworldindata.org/emissions-by-sector.
4. Kittner, N., Lill, F. & Kammen, D. M. Energy storage deployment and innovation for the clean energy transition. *Nature Energy* **2**, (2017).
5. Sun, H. & Zhao, K. Electronic Structure and Comparative Properties of $LiNi_xMn_yCo_zO_2$ Cathode Materials. *The Journal of Physical Chemistry C* **121**, 6002–6010 (2017).
6. Chen, X., Shen, W., Vo, T. T., Cao, Z. & Kapoor, A. An overview of lithium-ion batteries for electric vehicles. in *10th International Power and Energy Conference, IPEC 2012* 230–235 (2012). doi:10.1109/ASSCC.2012.6523269.
7. Besnard, N. *et al.* Multiscale Morphological and Electrical Characterization of Charge Transport Limitations to the Power Performance of Positive Electrode Blends for Lithium-Ion Batteries. *Advanced Energy Materials* **7**, (2017).
8. Molenda, J. Li-ion batteries for electric vehicles. *Annales UMCS, Chemistry* **66**, (2011).
9. The Internal Structure of Lithium Polymer Battery. https://www.ludabattery.com/the-internal-structure-of-lithium-polymer-battery/.
10. Badot, J. C., Lestriez, B. & Dubrunfaut, O. Interest in broadband dielectric spectroscopy to study the electronic transport in materials for lithium batteries. *Materials Science and Engineering B: Solid-State Materials for Advanced Technology* **213**, 190–198 (2016).
11. Noh, H. J., Youn, S., Yoon, C. S. & Sun, Y. K. Comparison of the structural and electrochemical properties of layered $Li[Ni_xCo_yMn_z]O_2$ (x = 1/3, 0.5, 0.6, 0.7, 0.8 and 0.85) cathode material for lithium-ion batteries. *Journal of Power Sources* **233**, 121–130 (2013).
12. Lipson, A. L. *et al.* Stabilizing NMC 811 Li-Ion Battery Cathode through a Rapid Coprecipitation Process. (2021) doi:10.1021/acsaem.0c03112.
13. Wang, S., Yan, M., Li, Y., Vinado, C. & Yang, J. Separating electronic and ionic conductivity in mix-conducting layered lithium transition-metal oxides. *Journal of Power Sources* **393**, 75–82 (2018).
14. Goodenough, J. B. & Kim, Y. Challenges for rechargeable Li batteries. *Chemistry of Materials* vol. 22 587–603 Preprint at https://doi.org/10.1021/cm901452z (2010).
15. Tamirat, A. G., Guan, X., Liu, J., Luo, J. & Xia, Y. Redox mediators as charge agents for changing electrochemical reactions. *Chemical Society Reviews* vol. 49 7454–7478 Preprint at https://doi.org/10.1039/d0cs00489h (2020).
16. Baker McKenzie. *Battery Storage-a global enabler of the Energy Transition 2022*. (2022).
17. Chen, Y. H., Wang, C. W., Zhang, X. & Sastry, A. M. Porous cathode optimization for lithium cells: Ionic and electronic conductivity, capacity, and selection of materials. *Journal of Power Sources* **195**, 2851–2862 (2010).
18. Hamed, H. *et al.* Demystifying Charge Transport Limitations in the Porous Electrodes of Lithium-Ion Batteries. *Advanced Energy Materials* **10**, (2020).
19. Dedryvère, R. *et al.* Electrode/electrolyte interface reactivity in high-voltage spinel $LiMn_{1.6}Ni_{0.4}O_4$/$Li_4Ti_5O_{12}$ lithium-ion battery. *Journal of Physical Chemistry C* **114**, 10999–11008 (2010).

20. Seid, K. A. *et al.* An in situ multiscale study of ion and electron motion in a lithium-ion battery composite electrode. *Advanced Energy Materials* **5**, (2015).
21. Woodward, W. H. H. Broadband Dielectric Spectroscopy - A Practical Guide. in *ACS Symposium Series* vol. 1375 3–59 (American Chemical Society, 2021).
22. Seid, K. A. *et al.* Multiscale electronic transport in $Li_{1+x}Ni_{1/3-u}Co_{1/3-v}Mn_{1/3-w}O_2$: A broadband dielectric study from 40 Hz to 10 GHz. *Physical Chemistry Chemical Physics* **15**, 19790–19798 (2013).
23. Agrawal, A. *et al.* Influence of a Liquid Electrolyte on Electronic and Ionic Transfers in a $LiNi_{0.5}Mn_{0.3}Co_{0.2}O_2$/Poly(vinylidene Fluoride- co-hexafluoropropylene)-Based Composite Material. *Journal of Physical Chemistry C* **125**, 17629–17646 (2021).
24. Böttcher, C. J. F., Bordewijk, P. & Rip, A. *Theory of electric polarization*. (Elsevier Scientific Pub. Co, 1973).
25. Belhadj-Tahar, N.-E. & Fourrier-Lamer, A. Broad-Band Analysis of a Coaxial Discontinuity Used for Dielectric Measurements. *346 IEEE Transactions On Microwave Theory And Techniques* vol. 34 (1986).
26. Sadou, H. *et al.* An approach based on ANFIS and input selection procedure for microwave characterization of dielectric materials. *COMPEL - The International Journal for Computation and Mathematics in Electrical and Electronic Engineering* **37**, 799–813 (2018).
27. Belhadj-Tahar, N.-E., Fourrier-Lamer, A. & de Chanterac, H. Broad-Band Simultaneous Measurement of Complex Permittivity and Permeability Using a Coaxial Discontinuity. *IEEE Transactions On Microwave Theory And Techniques* vol. 38 (1990).
28. Panabière, E., Badot, J. C., Dubrunfaut, O., Etiemble, A. & Lestriez, B. Electronic and Ionic Dynamics Coupled at Solid-Liquid Electrolyte Interfaces in Porous Nanocomposites of Carbon Black, Poly(vinylidene fluoride), and γ-Alumina. *Journal of Physical Chemistry C* **121**, 8364–8377 (2017).